J. Fluid Mech. (2011), *vol.* 681, *pp.* 411–433.
doi:10.1017/jfm.2011.205

Three-dimensional instabilities in the boundary-layer flow over a long rectangular plate

HEMANT K. CHAURASIA AND MARK C. THOMPSON†

Fluids Laboratory for Aeronautical and Industrial Research (FLAIR), Department of Mechanical and Aerospace Engineering, Monash University, Clayton, VIC 3800, Australia

(Received 1 September 2010; revised 6 March 2011; accepted 4 May 2011; first published online 16 June 2011)

A detailed numerical study of the separating and reattaching flow over a square leading-edge plate is presented, examining the instability modes governing transition from two- to three-dimensional flow. Under the influence of background noise, experiments show that the transition scenario typically is incompletely described by either global stability analysis or the transient growth of dominant optimal perturbation modes. Instead two-dimensional transition effectively can be triggered by the convective Kelvin–Helmholtz (KH) shear-layer instability; although it may be possible that this could be described alternatively in terms of higher-order optimal perturbation modes. At least in some experiments, observed transition occurs by either: (i) KH vortices shedding downstream directly and then almost immediately undergoing three-dimensional transition or (ii) at higher Reynolds numbers, larger vortical structures are shed that are also three-dimensionally unstable. These two paths lead to distinctly different three-dimensional arrangements of vortical flow structures. This paper focuses on the mechanisms underlying these three-dimensional transitions. Floquet analysis of weakly periodically forced flow, mimicking the observed two-dimensional quasi-periodic base flow, indicates that the two-dimensional vortex rollers shed from the recirculation region become globally three-dimensionally unstable at a Reynolds number of approximately 380. This transition Reynolds number and the predicted wavelength and flow symmetries match well with those of the experiments. The instability appears to be elliptical in nature with the perturbation field mainly restricted to the cores of the shed rollers and showing the spatial vorticity distribution expected for that instability type. Indeed an estimate of the theoretical predicted wavelength is also a good match to the prediction from Floquet analysis and theoretical estimates indicate the growth rate is positive. Fully three-dimensional simulations are also undertaken to explore the nonlinear development of the three-dimensional instability. These show the development of the characteristic upright hairpins observed in the experimental dye visualisations. The three-dimensional instability that manifests at lower Reynolds numbers is shown to be consistent with an elliptic instability of the KH shear-layer vortices in both symmetry and spanwise wavelength.

Key words: absolute/convective instability, vortex instability, vortex shedding

† Email address for correspondence: mark.thompson@eng.monash.edu.au

1. Introduction

The flow past a two-dimensional (2D) large aspect ratio rectangular plate (or cylinder) represents a generic flow problem with applications to industrially relevant flows such as heat exchanger plates and buildings. At Reynolds numbers above approximately 100 ($Re = U_\infty H/\nu$, where U_∞ is the upstream velocity, H the plate thickness and ν the kinematic viscosity), the flow separates at the leading edge and reattaches further downstream forming a steady separation bubble. As the Reynolds number is increased, Kelvin–Helmholtz (KH) waves may become visible depending on background noise levels, and the recirculation bubble begins to shed releasing large-scale vortex structures that advect downstream. This shedding is characteristic of many wall-bounded separating/reattaching flows, such as flow past a backward-facing step (Kaiktsis, Karniadakis & Orszag 1996; Barkley, Gomes & Henderson 2002; Blackburn, Barkley & Sherwin 2008*a*), flows over bumps (Marquet *et al.* 2008, 2009) and flows through stenotic geometries (Griffith *et al.* 2008; Blackburn, Sherwin & Barkley 2008*b*; Griffith *et al.* 2010).

This particular flow has been examined by a number of researchers over many years. Lane & Loehrke (1980); Ota, Asano & Okawa (1981); Sasaki & Kiya (1991) examined the transition to unsteady flow experimentally, finding it occurred over a Reynolds number range $260 < Re < 330$. Prior to this, the flow is steady with a recirculation bubble formed from the separating and reattaching shear layer. The flow is strongly three-dimensional (3D) post-transition. Tafti & Vanka (1991) examined the 2D flow numerically, determining the separation bubble length as a function of Reynolds number in agreement with the experimental results. Lane & Loehrke (1980); Sasaki & Kiya (1991) noted the role of KH instability waves in the transition process. Sigurdson (1995); Sigurdson & Roshko (1984); Sasaki & Kiya (1991) reported on the staggered arrangement of hairpin vortices observed as part of the transition process. These 3D hairpins continue to be visible at much higher Reynolds numbers. Hwang, Sung & Hyun (2001, 2000) examined the shear-layer flapping and shedding using high-speed imaging both for the unforced and forced cases. A number of authors have examined the locking of leading-edge shedding through a feedback loop involving the upstream pressure pulse as released vortices pass the trailing edge of the plate (e.g. Nakamura, Ohya & Tsurata 1991; Ohya *et al.* 1992; Hourigan, Thompson & Tan 2001; Mills, Sheridan & Hourigan 2003; Tan, Thompson & Hourigan 2004).

Such flows used to be considered to be *convectively unstable*, meaning that perturbations could grow in magnitude as they are convected downstream, but at any fixed position the perturbation would die away. Over the last 10 years or so, another interpretation has been put forward in terms of transient growth of optimal initial perturbations, i.e. certain initial spatial perturbation distributions are massively amplified as they advect downstream, possibly resulting in energy amplification factors of many orders of magnitude. This can happen even if the flow is globally stable because of the non-normality of the global modes, traced back to the convection term in the Navier–Stokes equations being not self-adjoint. This helps explain effective turbulent transition in Couette flow, which is globally stable, and early transition for a number of other flows such as pipe flow (Butler & Farrell 1992; Trefethen *et al.* 1993; Reddy & Henningson 1993). Thus it appears that transition can occur through transient amplification of optimal perturbation modes followed by nonlinear evolution but triggered by low-level background noise. For related flows, various authors have shown through direct simulations that low-level background noise is sufficient to trigger quasi-periodic flapping of the separating/reattaching shear layer, similar to that observed in experiments (Kaiktsis *et al.* 1996; Blackburn *et al.* 2008*a*).

Also of interest is that for some flows where the overall amplification of optimal perturbation modes is not too large, highly resolved direct numerical simulations (DNSs) have predicted that the irregular shedding transition is due to the almost simultaneous emergence of a set of global temporal instability modes, with frequencies differing by a fixed increment. Acting together this set of modes are subject to *beating*, which manifests as quasi-periodic flapping of the shear layer (Ehrenstein & Gallaire 2008; Cherubini, Robinet & Palma 2010), again similar to what is observed experimentally. Intriguingly, the global temporal modes appear to be similar in spatial structure to the evolved optimal perturbation modes.

A previous paper by Thompson (2010) examined the transient growth of optimal perturbation modes for this flow geometry. That paper indicated that the energy amplification of the optimal perturbation mode at $Re = 350$ was more than 4 orders of magnitude, and increases by 2.5 orders of magnitude for each Reynolds number increment of 100. The most-amplified optimal mode was 3D with a spanwise wavelength of $12H$. This indicates that preventing transition to unsteady flow in experiments becomes progressively more difficult since even very low-level noise is likely to trigger transition. Also of relevance, that paper also examined the 2D and 3D global instabilities. The steady flow becomes three-dimensionally unstable at $Re \simeq 390$ to a steady instability mode with a wavelength of approximately $16H$. The steady 2D flow does not undergo time-dependent transition until $Re \simeq 500$.

In terms of experiments, it is not at all likely that the background noise spectrum will be flat. Typically there is likely to be some frequency dependence, and perhaps preferred frequencies, such as the blade passing tone of the fan or pump. This may mean periodic forcing of spatial perturbations, which may be considered to be periodically projected onto the optimal perturbation modes, but not necessarily the most-amplified one(s) over all time periods. For instance, optimal modes corresponding to shorter amplification times tend to resemble shorter wavelength KH waves during their subsequent advection along the shear layer. It seems reasonable that if the background noise level is sufficiently high, the evolving perturbation fields will become nonlinear as they travel downstream. The experimental results of Sasaki & Kiya (1991) are a case in point. Over the Reynolds number range $320 < Re < 380$, they find that KH vortices are released from the separation zone into the downstream flow. These vortex filaments rapidly become three-dimensionally unstable during transit. They consist of lambda-shaped vortices and are in phase from one row to the next. They call this type of 3D shedding *Pattern A*. At higher Reynolds numbers, $Re > 380$, larger scale vortex structures are released from the recirculation zone and advect downstream. These are also three-dimensionally unstable – although producing a different 3D arrangement than for the first regime. The 3D structures then consist of hairpin-shaped vortices with the leading loop much less pointy than for Pattern A. The phasing is also different with the alignment of the hairpins offset by 180° from one row to the next. They call this arrangement *Pattern B*. Pattern B has also been observed by others independently in other studies including Kiya, Sasaki & Yasakawa (1983); Sigurdson & Roshko (1984); Kiya & Sasaki (1985); Sigurdson (1995).

An aim of the present paper is to examine the global 3D stability of these 2D vortices during formation and subsequent advection downstream. Experiments indicate that these shed vortices are immediately unstable three-dimensionally on formation, and hence this is an intrinsic part of the transition process. In order to do this, a low-level cross-stream oscillatory forcing is used to enforce periodic shedding from the recirculation zone, mimicking the underlying quasi-periodic shedding observed in the experiments. Then given a periodic base flow, Floquet stability analysis is used to

determine the 3D stability. Of interest is the physical mechanism underlying the instability. Finally 3D simulations are used to explore the nonlinear evolution of the advecting 3D structures.

2. Methodology

The flow over a bluff plate is modelled by the incompressible Navier–Stokes equations in an accelerating reference frame combined with the continuity constraint,

$$\frac{\partial \boldsymbol{u}}{\partial t} + \boldsymbol{u}\cdot\nabla\boldsymbol{u} = -\nabla p + \nu\nabla^2\boldsymbol{u} - \frac{\mathrm{d}\boldsymbol{u}_f}{\mathrm{d}t}, \tag{2.1}$$

and

$$\nabla\cdot\boldsymbol{u} = 0. \tag{2.2}$$

Here, p is the kinematic pressure, i.e. the pressure divided by the density, ν is the kinematic viscosity, and $\boldsymbol{u}$ is the velocity vector in the reference frame of the plate. The frame acceleration is given by $\mathrm{d}\boldsymbol{u}_f/\mathrm{d}t$. In this case, it is used to apply a small vertical sinusoidal oscillation to the plate to determine the effect on the shear-layer stability. These equations are solved numerically using a high-order spectral-element method of the kind first presented by Patera (1984). The method and developed software have been applied previously to various related problems, such as the wakes of cylinders (Thompson, Hourigan & Sheridan 1996; Thompson, Leweke & Williamson 2001*b*; Leontini, Thompson & Hourigan 2007), spheres (Thompson, Leweke & Provansal 2001*a*) and tori (Sheard, Thompson & Hourigan 2003, 2004). These previous studies provide confidence in the implementation and provide guidance for mesh requirements to resolve flow features. In contrast to finite-difference methods, which solve for flow variables only at discrete grid points, spectral-element methods compute the flow variables in terms of high-order piecewise Lagrangian polynomial interpolation functions which are continuous over all elements of the flow domain. The spectral-element method has been shown to achieve spectral or exponential convergence as the polynomial order within macro-elements is increased (e.g. Karniadakis & Sherwin 1999), but also allows the h refinement of h–p methods, allowing considerable flexibility with mesh construction. Since descriptions of the approach can be found in the series of papers mentioned above, only relevant specific details will be presented in this paper.

An essential component of any numerical study of fluid flow is the design of an efficient computational mesh. This problem is relatively expensive in computational terms because of the sizeable regions with large velocity gradients requiring high resolution. In particular, there are geometric singularities at the leading edges and relatively fine boundary layers extending all the way to the outflow boundary. After several attempts, a mesh was designed which had sufficient resolution in the regions where complex flow features occur, particularly towards the leading edge and within 1–2H of the plate surface, while limiting the concentration of macro-elements elsewhere.

The boundary conditions for the stationary plate case are $\boldsymbol{u} = \boldsymbol{0}$ at the surface of the plate, $\boldsymbol{u} = (U_\infty, 0)$ at the inflow and side boundaries and $\partial u/\partial x = \partial v/\partial x = 0$, i.e. a zero normal gradient condition, at the outflow boundary. For the case when the flow is perturbed by applying a vertical sinusoidal oscillation to the plate, the frame of reference is attached to the plate. Then the velocity is still set to zero at the plate surface, and the time-varying sinusoidal vertical perturbation velocity component is subtracted from the free stream velocity at the inflow and side boundaries to account for switching to the accelerating frame. Finally, for the Floquet analysis, described

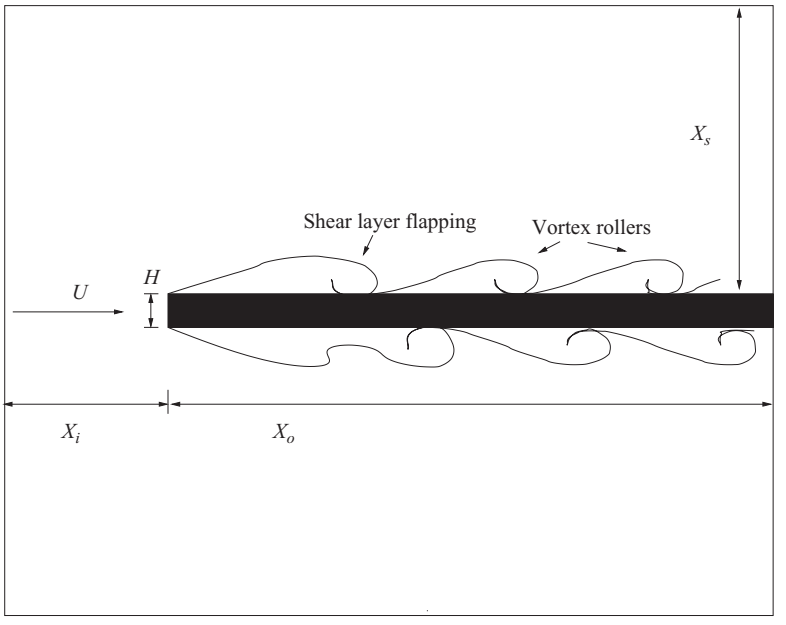

FIGURE 1. Problem setup: fluid flows past a bluff flat plate at upstream velocity U. Above a certain Reynolds number, the separating and reattaching shear layer flaps releasing large-scale vortex structures (rollers) that shed downstream.

below, zero perturbation velocity boundary conditions are used at all boundaries except outflow, where the zero normal gradient condition is again used.

Figure 2 shows the mesh used for the bulk of the simulations. In terms of the parameters shown in figure 1, this mesh has dimensions: inflow length $X_i = 10H$; plate length $X_o = 30H$; and top and bottom boundaries at $X_s = \pm 20H$. Resolution studies were performed to check grid independence by increasing the polynomial order within each macro-element until convergence was achieved. This was determined by monitoring the velocity at a point downstream of the mean reattachment length. It was found that convergence was achieved using 8×8 internal nodes per element, giving predictions of velocity maxima accurate to within 1 % of more highly resolved simulations.

Given a 2D base flow, the global stability can be established using linear stability analysis. A particular case of interest for this paper is when the base flow is periodic. In this case, the particular type of linear stability analysis is called Floquet stability analysis, which establishes whether or not a global perturbation will grow in time (exponentially) from one period to the next. This determines whether the base flow is globally or asymptotically stable or unstable. Typically, the control parameter is the Reynolds number. As the Reynolds number increases, at some stage the 2D periodic flow may become unstable as a 3D perturbation grows linearly until the flow saturates nonlinearly, typically resulting in a periodic or possibly quasi-periodic 3D flow. This analysis was applied to the circular cylinder wake by Barkley & Henderson (1996), indicating that the initial instability mode, called Mode A, becomes unstable at a Reynolds number of approximately 190. This fastest growing mode has a wavelength of about four cylinder diameters, and the transition is *subcritical*, meaning it is hysteretic. There is some supporting evidence that the instability is linked to the generic elliptic instability mechanism that occurs in strained elliptical vortices, i.e. it is primarily an instability of the vortex cores (Leweke & Williamson 1998*b*; Thompson

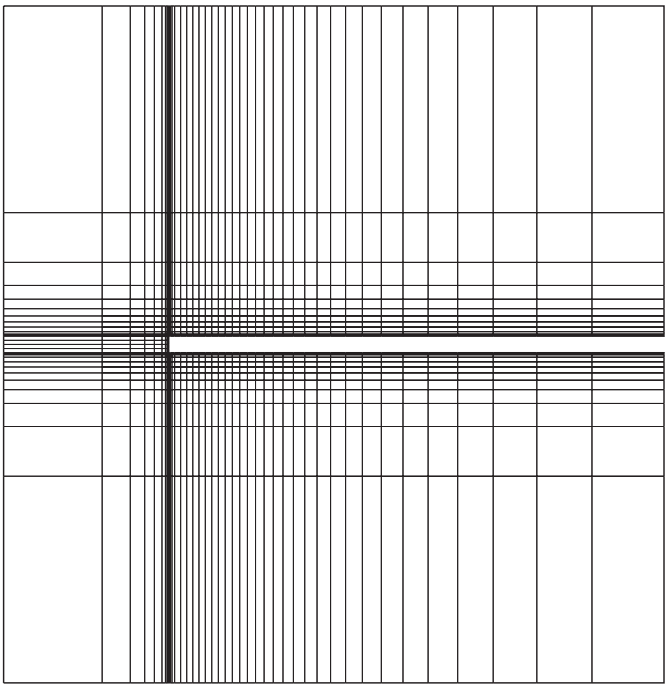

FIGURE 2. Typical computational mesh employed for the time-dependent simulations. This shows only the *macro-elements*, which were further subdivided into $N \times N$ nodes.

et al. 2001*b*; Julien, Ortiz & Chomaz 2004). A shorter wavelength ($\lambda \simeq 1D$) secondary instability occurs at a Reynolds number of approximately 260 on the unperturbed 2D base flow. This mode is known as Mode B, and the remnants of this instability mode appear to be observable in much higher Reynolds number wake flows (Wu *et al.* 1996), while the existence of Mode A at higher Reynolds numbers is more difficult to detect. (This may be because Mode A is unstable over an increasingly larger wavelength band at higher Reynolds numbers, so its appearance may be masked as seemingly random 3D motions.) Evidence has been put forward that the Mode B is associated with an instability of the braids between the Strouhal vortices (Williamson 1996) where the amplitude is strong, and more recently centrifugal instability has been implicated in its onset (Ryan, Thompson & Hourigan 2005). Blackburn & Lopez (2003*b*) have also linked braid-type instabilities to centrifugal instability for periodically driven cavities.

As presented by Barkley & Henderson (1996), the technique as applied here is based on evolving the 3D perturbation fields for the velocity and pressure forward in time. This is done for a series of Reynolds numbers over a selection of spanwise wavelengths (λ). Because the coefficients of the equations do not depend on the spanwise coordinate (z), the variation in the spanwise direction of the perturbation field can be represented as a Fourier expansion and the behaviour of each mode can be examined separately. In practice, the first few fastest growing eigenmodes contributing to the perturbation fields can be determined for each (λ, Re) by integrating in time from random perturbation fields, and renormalising the fields after each period if necessary to prevent unbounded growth. After sufficient time, typically 50–100 base flow periods, only the fastest growing or slowest decaying eigenmodes contribute to the perturbation field. Arnoldi decomposition (Barkley & Henderson 1996) can then be used on a set of stored perturbation fields to give good representations of the first

few dominant modes. The growth in amplitude of each eigenmode from one period to the next can also be extracted using the mode orthogonalisation procedure. These can be expressed as a (possibly complex) amplitude multiplier, commonly called a Floquet multiplier, μ, or a growth rate, σ, such that $\mu = \exp(\sigma T)$, where T is the base flow period. If the dominant multiplier is real, this means that the perturbation field has the same period as the base flow. If it is complex, then the eigenmodes form a complex pair and the eigenmode pair has a period that is different from the base flow period (Blackburn & Lopez 2003*a*). In any case, the values of μ as a function of λ and Re fully describe the *global* stability of a 2D periodic flow to 3D perturbations. If the magnitude of the dominant Floquet multiplier is less than unity, the mode exponentially decays over time and will not be observed in a real flow. The mathematical details of this procedure are not given here because they have been reported extensively elsewhere, e.g. Barkley & Henderson (1996); Ryan *et al.* (2005); Blackburn & Lopez (2003*a*).

3. Results

3.1. *2D base flow*

As indicated in the discussion above, the separating shear layer is very sensitive to external perturbations. For *finite-length* plates, at Reynolds numbers above a few hundred, the passage of previously released vortices from the leading-edge shear layer past the trailing edge is sufficient to maintain a feedback loop causing strong quasi-regular leading-edge shedding (Nakamura *et al.* 1991; Ozono *et al.* 1992; Tan, Thompson & Hourigan 1998; Hourigan *et al.* 2001). The mechanism is through a pressure pulse as the vortex passes the trailing edge, which perturbs the upstream shear layer completing the feedback loop. However, the case examined in this paper is that of flow past a semi-infinite plate, so that there can be no sudden upstream influence as vortices travel downstream along the plate. In practice this is difficult to achieve using the numerical model because the domain needs to be truncated at some point. The truncation has a similar effect to using a finite-length plate in that, as the vortices exit the domain, this can perturb the upstream shear layer causing it to roll up. So one requirement is to use a sufficiently long domain so that exiting of vortices through the outflow boundary does not prevent the flow smoothly settling down to a stable steady separating–reattaching flow when no cross-stream forcing is applied. With the current setup using a plate length of $(X_o =)30H$, the flow evolves to a steady state for $Re \leqslant 450$.

Figure 3 shows the behaviour of the reattachment length with Reynolds number from the simulations. This figure also shows results from previous experimental (Lane & Loehrke 1980; Ota *et al.* 1981; Sasaki & Kiya 1991) and numerical studies (Tafti & Vanka 1991) for comparison. It indicates that for three different sets of experiments, the separation bubble becomes unstable in the Reynolds number range $260 < Re < 330$. Above this range, the data indicate the mean separation bubble length, which asymptotes at higher Reynolds numbers to between 4 and $5H$. As the Reynolds number is increased, the numerically predicted separation bubble lengths deviate somewhat from previous numerical predictions of Tafti & Vanka (1991). This may be due to the relatively small width of their domain of only $4H$ causing a significant blockage effect, even though they indicate that there was an explicit attempt to reduce this effect. Notably the current numerical predictions fall between the experimental results of Ota *et al.* (1981) and Sasaki & Kiya (1991); Lane & Loehrke (1980). Numerical simulations with a plate length of $60H$ and higher and

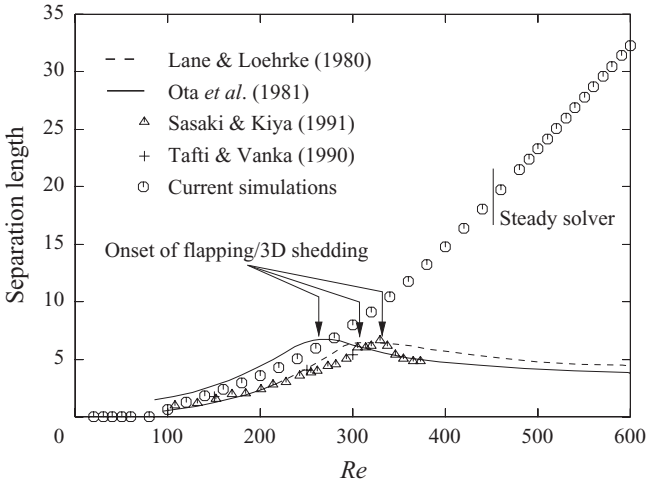

FIGURE 3. Reattachment length of the separation bubble as a function of Reynolds number. Results from various previous experimental and numerical studies are also given with the references supplied in the text. Where the experimental curves turn over, the flow undergoes transition to unsteady shedding.

lower polynomial resolutions made no difference to the predictions of the separation bubble lengths to graphical accuracy. Note that steady solutions could be obtained at much higher Reynolds numbers using a steady spectral-element flow solver based on a penalty formulation and Newton iteration. There was no difficulty in computing steady solutions for Reynolds numbers up to at least 1000. Some of these results are also shown in this figure. Note that in this case a bigger domain with a plate length of $60H$ was used, given the reattachment length exceeds $30H$ for $Re = 600$. For $Re < 400$, the variation of reattachment length with Reynolds number is above linear, while at higher Reynolds numbers the variation appears close to linear.

3.2. *Forced flow*

Thompson (2010) showed that the 2D flow undergoes an initial global transition to a steady 3D flow at $Re \simeq 393$, and that the global transition to unsteady flow occurs at $Re \simeq 500$. Importantly, both of these transitions occur at higher Reynolds numbers than effective transition is observed in experiments. In addition, Thompson (2010) also examined the transient growth of optimal perturbation modes showing that at $Re = 350$ energy growth is more than 4 orders of magnitude. This seems consistent with the experimental findings where background noise levels are likely to be sufficient to trigger early transition. Thus, while transient growth appears to provide a route to unsteady transition, experiments clearly show that the flow becomes both unsteady and 3D post-transition. It is also clear that experiments typically show (e.g. Sasaki & Kiya 1991) that shorter wavelength KH instability waves play a part. While the optimal 3D transient growth mode is amplified slightly more than the most amplified 2D mode, the corresponding preferred spanwise wavelength is approximately $12H$. This is much longer than the experimentally observed spanwise wavelength soon after onset of about $2H$ (Sasaki & Kiya 1991).

An hypothesised transition scenario is that the background noise feeds energy into KH waves or optimal initial perturbation modes which undergo rapid transient growth resulting in predominantly 2D shedding from the separation zone. This will be discussed further below. The released vortex rollers are then unstable to 3D

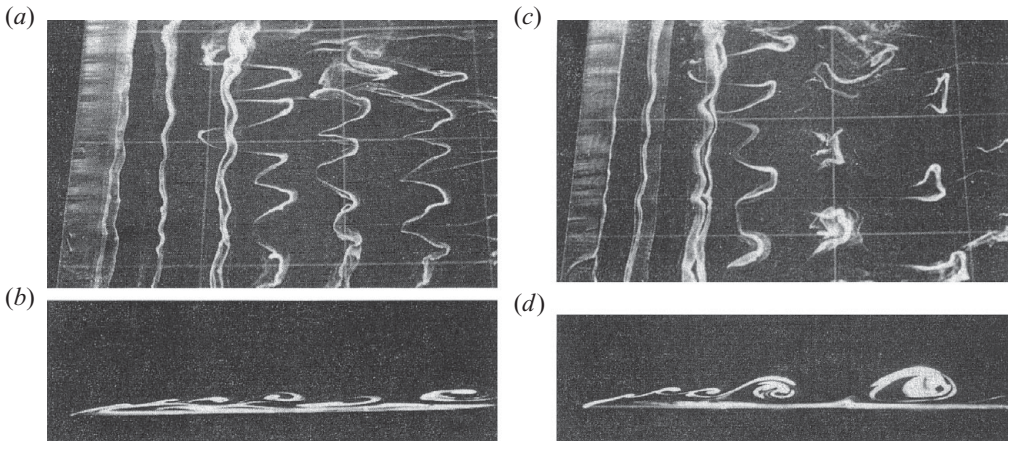

FIGURE 4. Experimental dye visualisations from Sasaki & Kiya (1991). (*a*) 3D vortex arrangement corresponding to Pattern A; (*b*) the shed vortices appear to be closely linked with KH vortices. (*c*) 3D structure for Pattern B; (*d*) the stronger shed vortices now arise from shear-layer flapping and merging of smaller KH vortices.

perturbations leading to the experimentally observed strongly 3D flow (see figure 4). Further, it can be speculated that the secondary (3D) instability is effectively a global instability of the quasi-periodic 2D flapping flow. In order to test this hypothesis, it seems reasonable to regularise the 2D quasi-periodic shedding by applying a very low-level sinusoidal cross-stream forcing to force periodicity. Then a Floquet analysis can be carried out on the strictly periodic flow to investigate the global stability.

A low amplitude sinusoidal forcing was applied perpendicular to the flow at the inlet and side boundaries, in order to make the shear-layer flapping and release of vortices strictly periodic. Initially this was done for a low-level forcing amplitude of $0.0005U$ over a range of forcing frequencies to determine the maximal response. Figure 5 shows a snapshot of the perturbation velocity field after sinusoidal forcing had been applied to the steady base flow for $1/4$ of a period, i.e. after the perturbation reaches the maximum amplitude. The effect is strongest near the leading-edge corners where it perturbs the shear layers as they separate. The vertical velocity component was recorded at a mesh point $(8.23H, 0.625H)$ well downstream of the leading edge to quantify the response. Figure 6 shows the non-dimensional response amplitude as a function of Strouhal number. The maximum response occurs close to $St = fH/U = 0.1$, where f is the frequency; however, the response drops off rapidly if the Strouhal number is reduced below this value, but it also shows some resonant peaks. The second peak from the left corresponds to forcing at half the preferred response frequency. The other peaks match frequency ratios of $1/3$ and $2/3$ times the preferred frequency. Above the Strouhal number corresponding to the maximal response, the response drops smoothly to zero as the forcing frequency is increased. From this analysis, it was decided to use a forcing frequency slightly higher than the maximal response frequency (i.e. $St = 0.11$) to ensure the excitation of the fundamental mode.

Subsequently, for a fixed forcing frequency of $St = 0.11$ and $Re = 400$, the downstream response was determined as a function of the input forcing amplitude between 0.0001 % and 1 % of the free stream velocity. The result is shown in figure 7. Clearly even at an extremely low forcing level of 0.001 % of the free stream velocity, the downstream flow is periodic reaching a non-negligible amplitude. The magnitude of the response is clarified further through figure 8, which shows greyscale vorticity

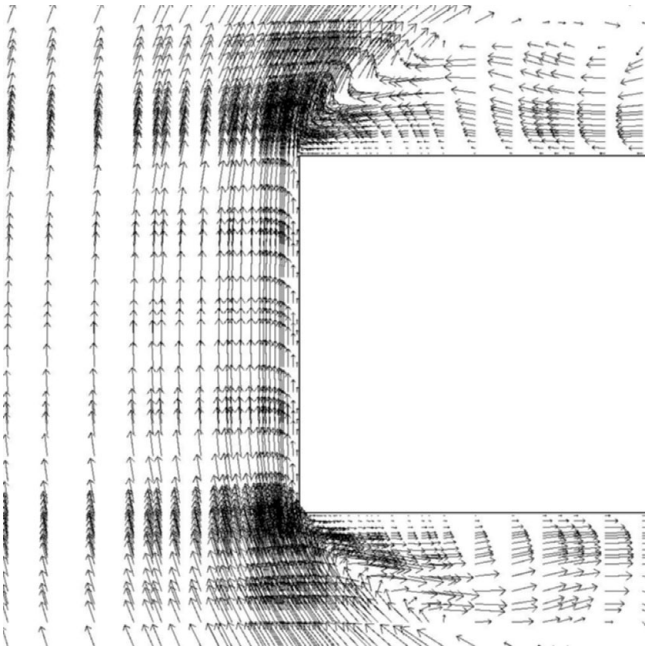

FIGURE 5. Perturbation velocity in the vicinity of the leading edge of the plate one quarter of period after low-level sinusoidal forcing was applied to the steady separated flow. Here $Re = 400$, $St = 0.11$, and the forcing amplitude is 0.05 %.

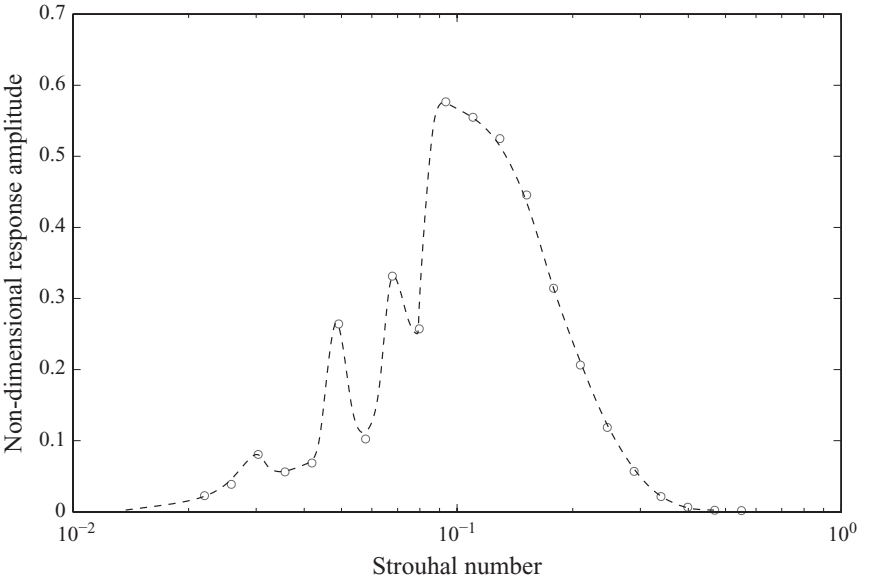

FIGURE 6. Frequency response of bluff plate boundary layer flow to varying frequencies of excitation. The forcing amplitude imposed on the flow is $0.0005U$, and peak flow response is observed close to $St = 0.1$.

plots for different input forcing amplitudes. It is also quite clear from these plots that a forcing level of 0.001 % is sufficient to produce weak periodic shedding from the separation zone. At higher forcing levels between 0.01 % and 0.1 %, the shed vortex rollers become compact and discrete. The separation zone is also shortened as the

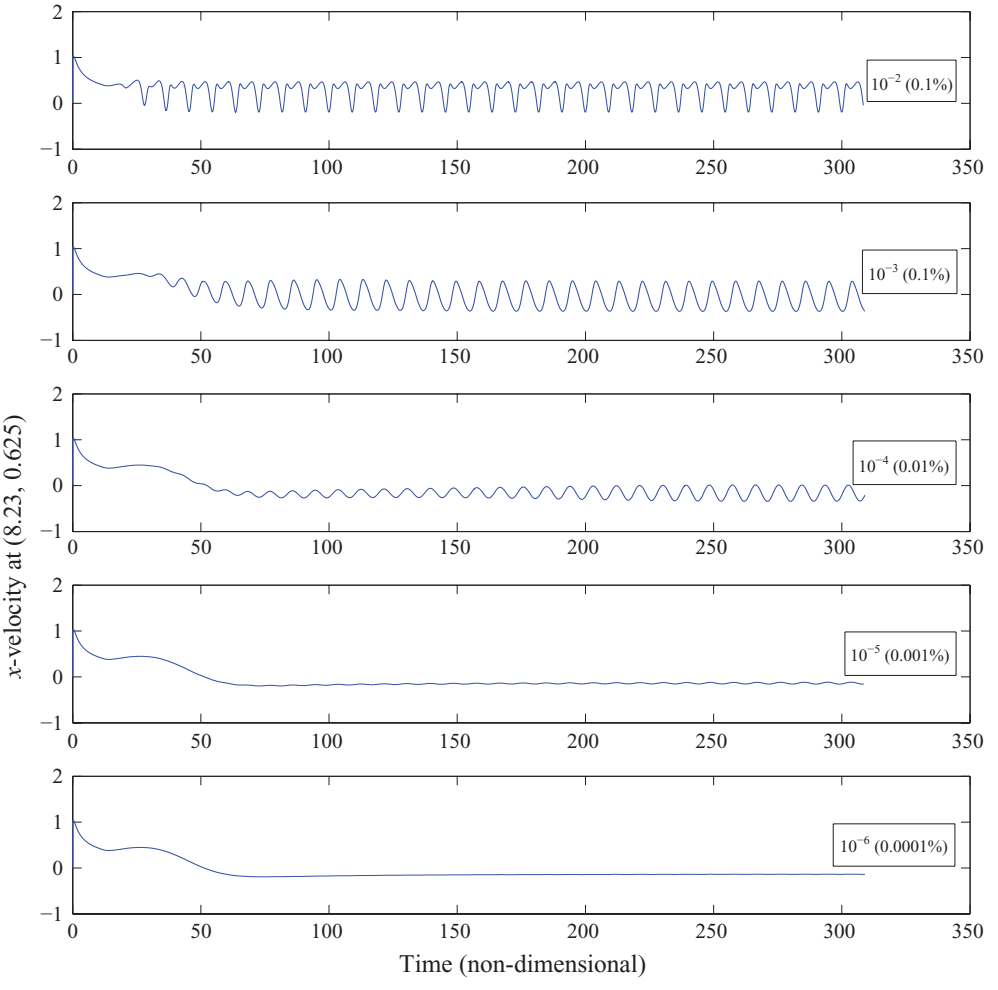

FIGURE 7. (Colour online available at journals.cambridge.org/FLM) Horizontal velocity component at a downstream point $(8.23H, 0.625H)$ caused by a low-level cross-stream sinusoidal oscillation. The input forcing amplitude is shown as an inset for each response curve. Here, $Re = 400$ and $St = 0.11$.

forcing amplitude is increased. At a forcing level of 1 %, very strong and compact vortices are produced.

3.3. *Floquet multipliers*

Given a periodic base flow, it is possible to determine the linear stability using Floquet analysis. This determines the stability of the 2D periodic flow to spanwise perturbations. In practice, for a given Reynolds number the first few global instability modes are determined corresponding to different spanwise wavelengths. The 2D flow is then unstable if any of the modes have positive growth rates. Alternatively *Floquet multipliers* can be used instead of growth rates. These are just the ratios of the mode amplitudes to their values one period prior. Figure 9 shows the Floquet multiplier curves as a function of spanwise wavelength for different Reynolds numbers. This is for a forcing level of 0.05 %. The two different peaks correspond to different spatial mode shapes. The curves indicate that the flow becomes three-dimensionally unstable

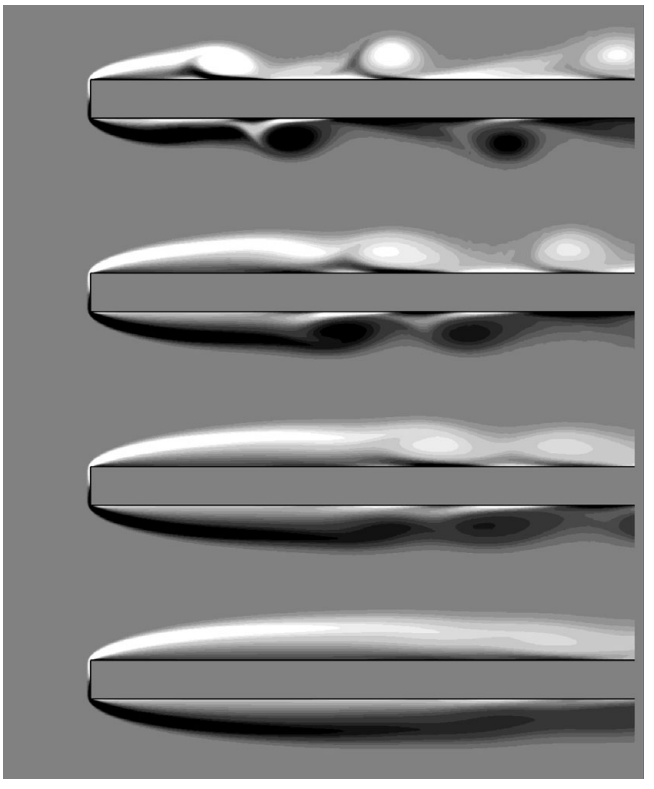

FIGURE 8. Vortex shedding induced by low-level cross-stream oscillatory forcing. The forcing levels from top to bottom are 1 %, 0.1 %, 0.01 % and 0.001 % of the upstream velocity. Here, $Re = 400$ and $St = 0.11$. All plots are at the same phase of the forcing cycle.

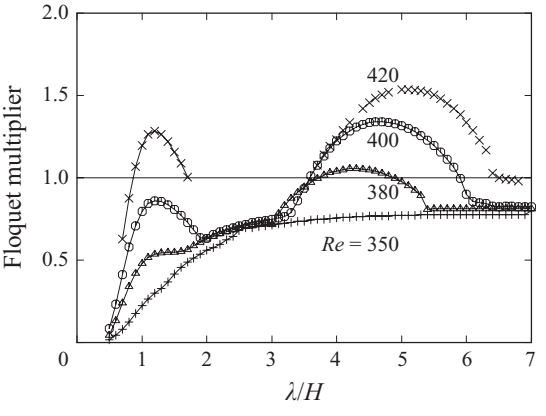

FIGURE 9. Floquet multiplier as a function of spanwise perturbation wavelength for different Reynolds numbers. Two distinct instability modes are observed, at $\lambda/H \approx 1.2$ and $\lambda/H \approx 4.2$, respectively. The forcing amplitude corresponds to 0.05 % of the free stream velocity.

between $Re = 350$ and 380 initially for a spanwise wavelength slightly greater than $4H$. At a slightly higher Reynolds number another shorter wavelength mode also becomes unstable. This has a wavelength of approximately $1.2H$.

The spatial structure of these two instability modes is revealed in figure 10. The top image is a greyscale plot of the spanwise vorticity field showing the vortices shed

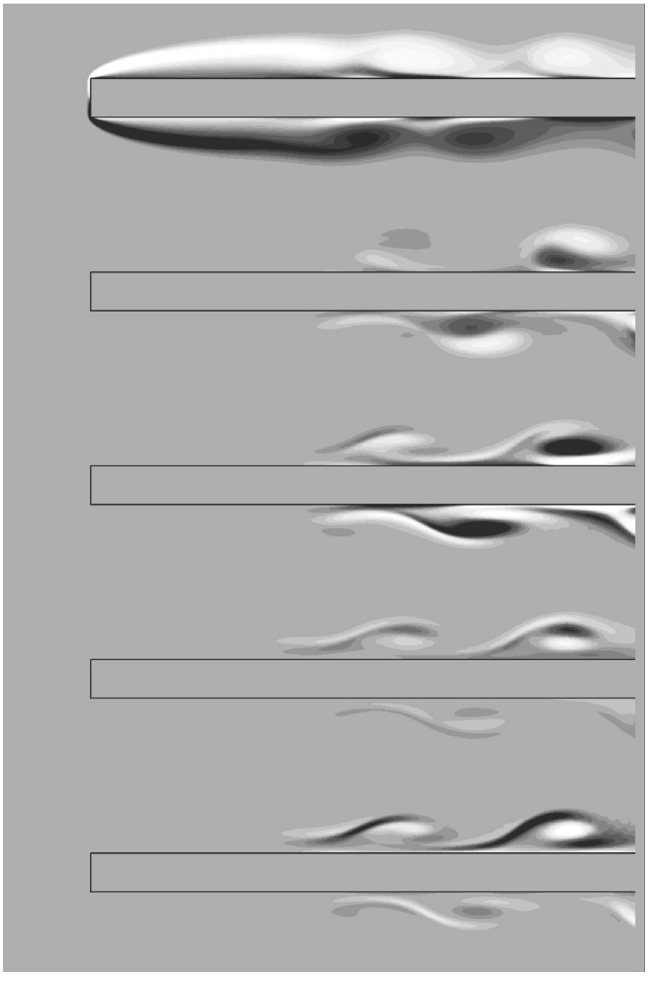

FIGURE 10. Spatial structure of the instability observed for a forcing level of 0.05 %. Top image is a greyscale plot of the spanwise vorticity for the periodic base flow. This shows the shear layer flapping and release of compact vortical structures. The next two images are the spanwise and streamwise perturbation vorticity for the longer wavelength instability. Finally the last two images show the spanwise and streamwise perturbation vorticity for the shorter wavelength instability. All images correspond to $Re = 400$.

from the separation bubble. The next two images show the spanwise and streamwise perturbation vorticity field for the longer wavelength mode. The perturbation field is clearly maximal in the vortex cores, and the spatial spanwise vorticity distribution is clearly indicative of elliptic instability, as discussed further below. The final two images show the spanwise and streamwise perturbation vorticity for the shorter wavelength mode. This appears to resemble a higher-order elliptic instability mode, corresponding to the same azimuthal wavenumber ($|m| = 1$) but a higher radial wavenumber ($n = 1$), i.e. one radial node. Of note is that the longer wavelength mode has a period of twice the forcing period. The instability reverses sign from one period to the next. This is consistent with experimental results for Pattern B.

Figure 11 provides evidence of the dominant elliptic nature of the instability. The top image shows the spanwise vorticity field, with the inset box showing the spatial domain of the next five images. Image (*b*) shows a zoomed-in view of the spanwise

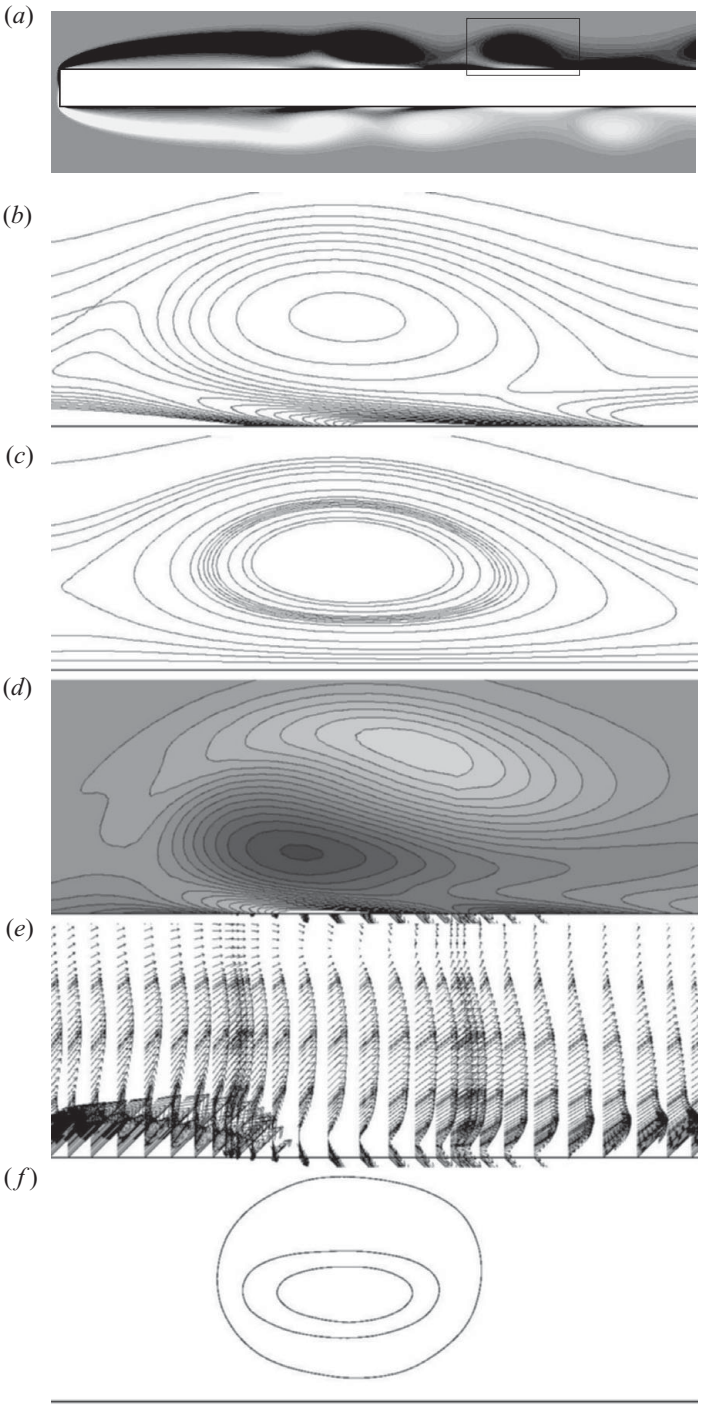

FIGURE 11. Evidence for elliptical nature of the instability. The images show: (*a*) spanwise vorticity of the forced flow, with the box indicating the region of focus for the other five images; (*b*) vorticity contours of the base flow; (*c*) streamlines in the frame attached to the convecting vortex; (*d*) perturbation spanwise vorticity from the numerical stability analysis; (*e*) vectors showing the direction and magnitude of the strain in the neighbourhood of the vortex core and (*f*) region of positive viscous growth from applying the idealised theory (contours correspond to growth rates of 0, 0.25, 0.28).

vorticity contours ($-2 < \omega_z H/U_\infty < 2$), while (*c*) shows streamlines in the frame-of-reference of the moving vortex structure, clearly showing elliptical streamlines as required for an elliptic instability. The major and minor axes of the ellipses are approximately aligned with the x (horizontal) and y (vertical) axes. The eccentricity is substantial. Image (*d*) is a close-up of the spanwise perturbation vorticity, showing the generic two-lobed structure characteristic of the $|m| = 1$, $n = 0$ mode. Here, n and m correspond to the radial and azimuthal wavenumbers defining the instability mode. Note that the centres of the lobes are aligned at approximately 45° to the axes of the streamline ellipses, along the direction of the principal strain as shown in image (*e*). This is the expected alignment for an idealised elliptic instability. Finally, the outer contour of image (*f*) shows the local region where the flow is elliptic in nature. This is governed by the parameter $\beta = 2\epsilon/|\omega|$, where ω is the vorticity and ϵ is the local strain rate. The flow is elliptic for $0 < \beta < 1$.

Various authors (Leweke & Williamson 1998*a*; Eloy & Le Dizes 1999) have shown that the most unstable mode of a finite-sized vortex core resemble the localised solutions for unbounded elliptical flow examined by Waleffe (1990). Hence there is a reasonable justification to examine more complex elliptical flows in terms of idealised theory. According to Landman & Saffman (1987), the growth rate in the idealised case of a flow with streamlines of constant eccentricity is given by a non-dimensionalised inviscid growth rate, σ_i, and a non-dimensionalised viscous damping rate, σ_ν, i.e.

$$\sigma = \sigma_i - \sigma_\nu, \tag{3.1}$$

where

$$\sigma_i \simeq \left(\epsilon \frac{H}{U}\right) \frac{9}{16}(1 - \beta^m)^n \tag{3.2}$$

and

$$\sigma_\nu = \frac{1}{Re}\left(\frac{2\pi}{(\lambda/H)}\right)^2 \frac{1 - \beta\cos^2\theta}{(1-\beta)\cos^2\theta}. \tag{3.3}$$

The expression for the inviscid growth rate is a least-squares fit to the numerically determined result of Landman & Saffman (1987) (see Leweke & Williamson 1998*b*), with the best-fit parameters determined to be $m = 2.811$ and $n = 0.3914$. The viscous damping term depends on θ, the angle of the wave vector of the most unstable perturbation with the rotation axis. The results from Landman & Saffman (1987, see figure 3) indicate that for $\beta < 0.6$, the most unstable wavenumber inclination is not a function of the wave vector-magnitude, while for larger values there is some variation with vorticity magnitude and amplitude. For the vortex depicted in figure 11, the value of β at the centre of the vortex is approximately 0.7. This restricts θ to lie approximately in the range of $43 < \theta < 50$, which means the growth rate at the centre of the vortices is predicted to lie between 0.30 and 0.32. Figure 11(*f*) shows contours of growth rate for the $\theta = 50°$ case. After the vortex has advected along the plate for a single period, the theoretical growth rate at the centre has dropped to approximately 0.25. Clearly, based on the idealised case, elliptic instability theory predicts strong amplification of an elliptic perturbation field. These numbers can be compared with the actual growth determined from the Floquet analysis. The difference in the magnitude of the perturbation field from its position shown in figure 11 to the magnitude of the next downstream vortex, i.e. the growth in one period measured moving with the vortex, is very close to a factor of 3. This translates to a growth rate of $\sigma = \log_e \mu/T = 0.12$. While this is significantly lower than the theoretical maximum growth rate measured at the centre of the vortex, it should not be surprising since,

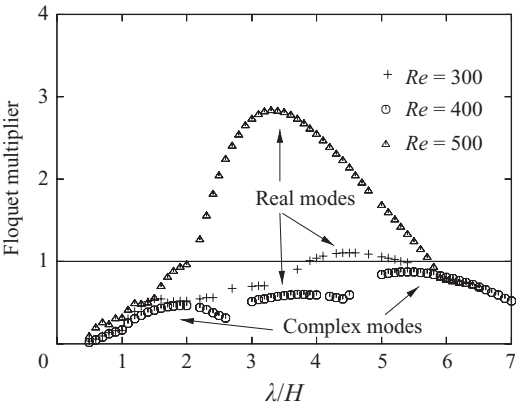

FIGURE 12. Floquet multiplier as a function of spanwise perturbation wavelength for different Reynolds numbers at a forcing amplitude of 0.5 % of the free stream velocity.

as shown in figure 11(*d*), a considerable fraction of the perturbation structure lies outside the region of maximum growth and even outside the elliptic region as shown in figure 11(*f*). Note that this *advective growth multiplier* is not the same as the Floquet multiplier, which just measures the growth multiplier over a period at a fixed point. The maximum Floquet multiplier at $Re = 400$ is 1.32, which is equivalent to a local growth rate of 0.032.

For a generic elliptic instability in the limit of vanishing strain the preferred wavelength is twice the geometric diameter of the invariant streamtube, i.e. the closed circuit where the perturbation velocity falls to zero. While this strictly does not happen in the real case, nevertheless the size of the vortex core region should give an appropriate estimate. For the just released vortex in the top image of figure 10, the major and minor axis lengths can be estimated as $3H$ and $1.3H$. This gives a geometric mean of close to $2H$ and hence indicates that the spanwise wavelength should be close to $4H$ if elliptic instability is the main cause of the complex 3D instability. This is, of course, very close to the preferred wavelength determined directly from Floquet stability analysis of $4.6H$ at $Re = 400$. Alternatively, for flows with elliptical streamlines without a restriction on the eccentricity Landman & Saffman (1987) give the preferred spanwise wavelength to be

$$\lambda = L\left(\frac{2}{1-\beta}\right)^{1/2}\tan\theta, \tag{3.4}$$

where L is the core length-scale, which for newly released vortices appears to be around $2H$ as discussed above. Given that $\beta \sim 0.7$, this gives $\lambda \sim 5H$, again close to the result from Floquet analysis.

3.3.1. *Effect of forcing amplitude*

Figure 12 shows the Floquet multiplier curves for a higher forcing amplitude of 0.5 % of the free stream velocity. In this case the shedding is stronger and the shed vortices are more compact and less elliptical, as can be seen from the trend shown in figure 8. The more compact shed vortex size reduces the core length-scale which in turn directly affects the preferred spanwise wavelength; thus at the higher forcing amplitude or higher Reynolds number the most amplified wavelength is reduced. This is consistent with the measured wavelength of Pattern B from the experiments of Sasaki & Kiya (1991) of 3–4H. At this higher forcing amplitude, the shorter

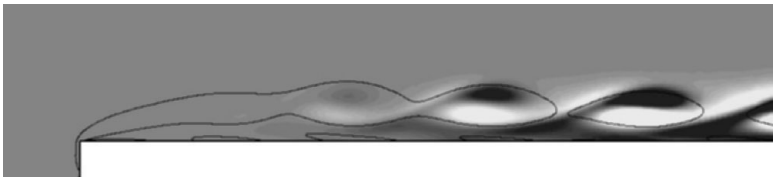

FIGURE 13. Floquet multiplier curves for the flow forced at $St = 0.22$ and $Re = 350$. The different curves correspond to different forcing amplitudes.

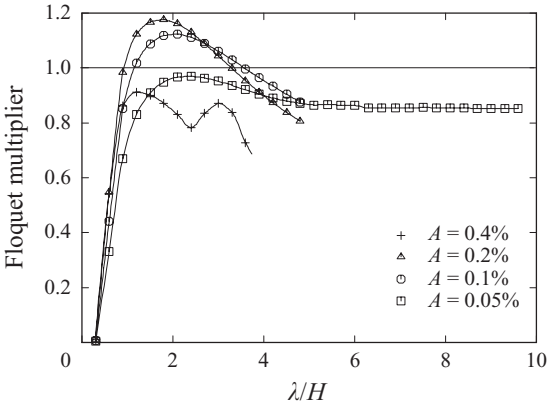

FIGURE 14. Greyscale plot of the spanwise perturbation vorticity corresponding to $Re = 350$, $\lambda_z = 1.8H$ at a forcing amplitude of 0.2 %. The solid lines show the base flow vorticity at $\omega_z = \pm 1.3$.

wavelength mode shown in figure 9 is suppressed, presumably because it is pushed to shorter wavelengths (as the core size is reduced) where viscous damping is stronger.

3.4. *Floquet analysis at a higher forcing frequency*

Figure 4 seems to indicate that Pattern A results when the KH shear-layer vortices shed directly, although there may be some merging further downstream. To investigate this further a base flow was generated using a forcing frequency of twice the previous case, i.e. $St = 0.22$. Some justification for this choice comes from the side-view images of figure 4, which appear consistent with the larger-scale vortices resulting from merging of pairs of higher frequency shear-layer vortices.

Figure 13 shows a plot of the spanwise perturbation vorticity at $Re = 350$ for the maximally amplified spanwise wavelength of $1.8H$ for a forcing amplitude of 0.2 %. The solid lines show vorticity contours of $\omega = \pm 1.3$ to highlight the positions of the shear-layer vortices. Once again the instability appears to manifest strongly in the vortex cores. Importantly the perturbation alignment is the same from one vortex to the next, in agreement with the downstream alignment of vortex loops observed experimentally.

Figure 14 shows the Floquet multiplier curves for various different forcing amplitudes at $Re = 350$, which is at the middle of the range over which Pattern A is observed. The results indicate that for forcing amplitudes of 0.1 % and 0.2 %, the Floquet multiplier becomes positive for wavelengths centred around $2H$. This is close to the observed Pattern A wavelength. At higher forcing amplitudes, the Floquet multiplier once again becomes less than one. This is presumably associated with the vortex cores becoming more compact under stronger forcing leading to a shorter

preferred spanwise wavelength; however, the viscous damping varies quadratically with the inverse of the core length-scale leading to overall damping. Note that for this Reynolds number even at these higher forcing amplitudes, the Floquet modes all decay for a forcing Strouhal number of $St = 0.11$.

Further evidence that this instability mode is associated with Pattern A shedding comes from 3D simulations examined below.

3.5. *Three-dimensional DNS calculations*

A series of fully 3D DNS were undertaken to explore the nonlinear evolution of these instabilities. These simulations employ a hybrid spectral-element/spectral code (Thompson *et al.* 1996). The extension to 3D is based on the same mesh and spectral-element representation used for the 2D simulations, with a Fourier representation in the spanwise direction. Details of the approach can be found in Karniadakis & Trintafyllou (1992). Of course, this enforces periodicity in the spanwise direction but also restricts the 3D variation to be expressed as a series of Fourier modes with discrete wavelengths. For our 3D simulations, the spanwise domain was chosen to be three times the wavelength of the observed dominant Pattern B instability, which is approximately $4.6H$ at $Re = 400$. Different simulations used up to 96 Fourier planes in the spanwise direction and the predictions were compared to verify that the flow was well resolved. Note that no dealiasing was used because of the low Reynolds number involved. A periodic forcing of $0.001U$ was applied at the inflow and side boundaries with $St = 0.11$, to duplicate the conditions of the 2D simulations. The flow was seeded with low-level random noise to initiate the development of three-dimensionality.

Different visualisations of the 3D simulated flow at $Re = 400$ are provided in figure 15. The top image shows vortical structures visualised using the method proposed by Jeong & Hussain (1995). This image shows the 3D structures post saturation. The middle and lower images are tracer particle plots at different stages in the evolution. The middle image shows a particle visualisation prior to saturation, before the vortex loops have become upright. The lower image shows a 3D structure post saturation. The vortex loops or hairpins are clearly visible and match up nicely with the experimental flow visualisation shown in figure 4 for Pattern B, in wavelength, phasing and overall structure. The numerical particle image at saturation bears a striking similarity to the experimental dye visualisation.

A 3D simulation was also performed for the instability mode occurring at higher frequencies but for lower Reynolds numbers, which shows characteristics of Pattern A. The same set-up was used as for Pattern B above, with $Re = 350$, $St = 0.22$ and with low-level random noise added to the initial field to initiate the growth of the instability. Figure 16 shows a particle tracer plot of the fully developed field, with the aligned loops clearly visible. The spanwise domain corresponds to $6H$ and shows three spanwise wavelengths of the fully developed mode.

4. Discussion and conclusions

For this flow, experiments seem to indicate that *in practice* transition to unsteady flow is intrinsically linked to 3D transition. Indeed Sasaki & Kiya (1991) find that transition is a two-stage process, with both stages marked by strongly 3D flow, both with preferred spanwise wavelengths far from those predicted by either global stability or transient growth analyses.

The analysis in this paper puts forward an interpretation of the experimentally observed transition. It could be expected that the optimal perturbation analysis should

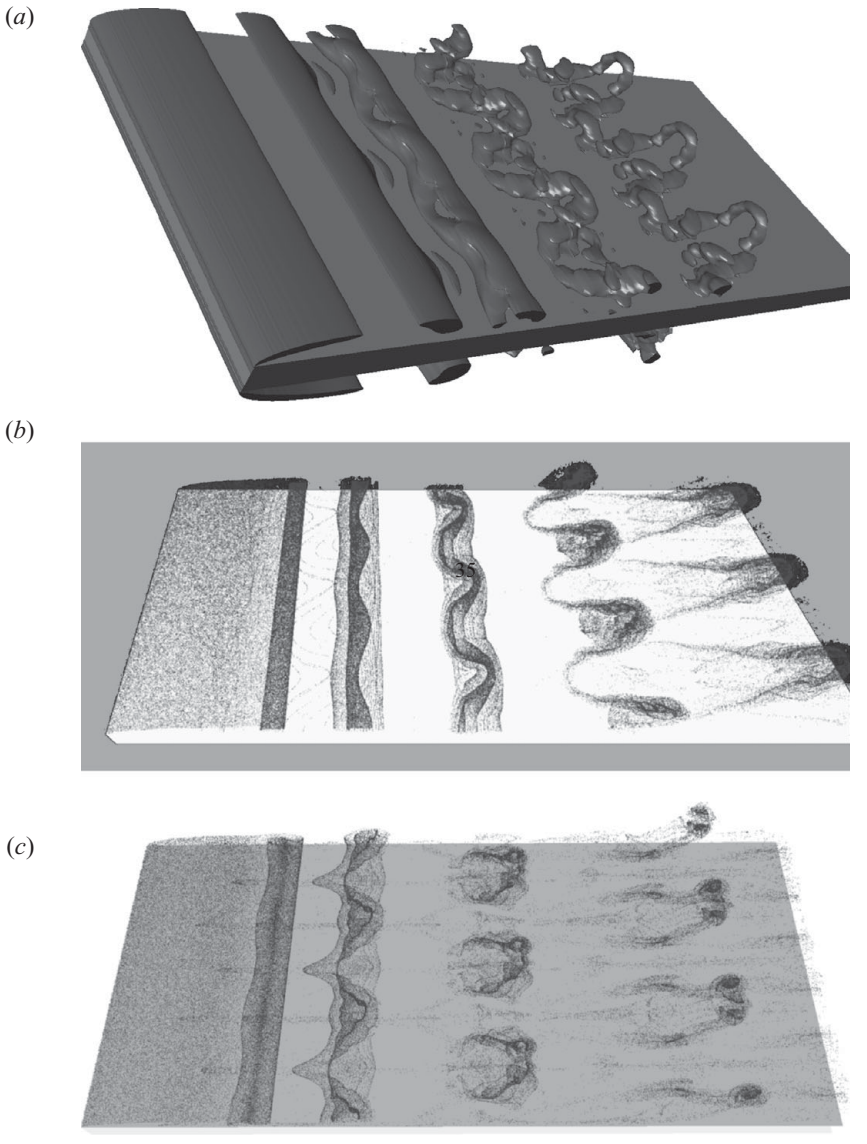

FIGURE 15. Visualisations of 3D structures from the direct simulations. (*a*) The vortical structures using the approach of Jeong & Hussain (1995). (*b*,*c*) Tracer particle simulations from the direct simulations that can be compared to figure 4(*c*) from experiments. The first (middle) of these images is shown at a time when the 3D mode is still developing. (*c*) A visualisation after the flow has saturated. The upright loops in the top and bottom images are quite striking, seeming to match the experimental observations in figure 4. Here, $Re = 400$.

describe the initial transition, since transient amplification is significant and transition occurs prior to the flow becoming globally unstable. However, the experiments of Sasaki & Kiya (1991) indicate that KH waves are involved in the initial transition. This probably indicates that the noise spectrum in the experimental rig is not flat but is shifted to higher frequencies, so that shorter wavelength KH waves are excited and grow preferentially, rather than the overall maximally amplified optimal perturbation mode, which does not seem to lead to the transient development of equivalent KH

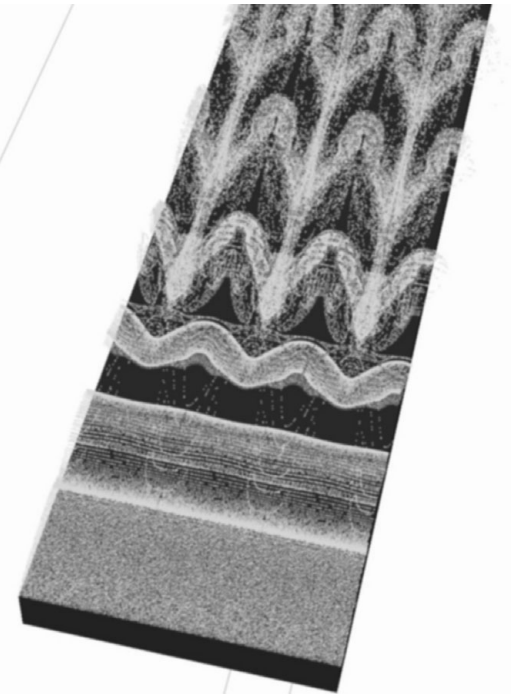

FIGURE 16. Visualisations of 3D structures resulting from perturbing the flow at twice the natural shedding frequency ($St = 0.22$) for $Re = 350$. Forcing amplitude was 0.2 %.

waves during nonlinear evolution (Thompson 2010). These KH vortices are released into the flow and appear to be three-dimensionally unstable resulting in the Pattern A mode. While this is not the main focus of the paper since it is not the mode that persists as the Reynolds number is increased, nevertheless an explanation for its development is provided. By forcing the flow at a frequency which excites the KH waves in the separating shear layer, the flow is shown to be unstable to 3D transition. The predicted spanwise wavelength and the downstream symmetry are consistent with Pattern A characteristics. The forcing amplitude range required for the instability to develop is also consistent with probable noise levels in the experiments.

The main analysis, however, focuses on the second transition at $Re > 380$. In that case the KH waves are still present, but their initial amplification is sufficient to cause nonlinear merging, so that much larger vortex rollers are released. The net effect, in terms of the release of large-scale vortex rollers, appears to be similar to the transient growth, nonlinear saturation and release of the optimal initial perturbation mode examined by Thompson (2010). Experiments show that semi-periodic shedding is maintained in this regime, presumably due to the background noise and possibly nonlinear feedback. This is similar to the quasi-periodic flapping and shedding observed in DNS for the backward-facing step (Blackburn *et al.* 2008*a*). So, to examine the 3D transition in this paper, a very low-level cross-stream oscillation is used to lock the shedding. Floquet stability analysis then indicates that the flow is three-dimensionally unstable for $Re > 380$. The predicted wavelength is approximately $4H$ at onset and so is consistent with experiments with measured wavelengths between 3 and $4H$. The phasing between rows of hairpin vortices from the Floquet analysis also matches the experimental arrangement. The stability analysis from this paper

shows that the perturbation field is maximal in the cores of the advecting vortex rollers and the perturbation field distribution is very reminiscent of elliptic instability. Indeed an estimate of the preferred wavelength from analytic theory gives a value of about $5H$ at onset, in line with the Floquet stability analysis and experiments. Finally, DNSs of the periodic base flow match the upright vortex hairpins observed in the experiments for Pattern B.

This research was conducted through the support of an Australian Postgraduate Award. We also acknowledge generous computing time support from the National Computing Infrastructure (NCI) facility at the ANU in Canberra, Australia.

REFERENCES

Barkley, D., Gomes, M. G. M. & Henderson, R. D. 2002 Three-dimensional instability in flow over a backward-facing step. *J. Fluid Mech.* **473**, 167–190.

Barkley, D. & Henderson, R. D. 1996 Three-dimensional Floquet stability analysis of the wake of a circular cylinder. *J. Fluid Mech.* **322**, 215–241.

Blackburn, H. M., Barkley, D. & Sherwin, S. J. 2008*a* Convective instability and transient growth in flow over a backward-facing step. *J. Fluid Mech.* **603**, 271–304.

Blackburn, H. M. & Lopez, J. M. 2003*a* On three-dimensional quasiperiodic Floquet instabilities of two-dimensional bluff body wakes. *Phys. Fluids* **15**, L57–L60.

Blackburn, H. M. & Lopez, J. M. 2003*b* The onset of three-dimensional standing and modulated travelling waves in a periodically-driven cavity flow. *J. Fluid Mech.* **497**, 289–317.

Blackburn, H. M., Sherwin, S. J. & Barkley, D. 2008*b* Convective instability and transient growth in steady and pulsatile stenotic flow. *J. Fluid Mech.* **607**, 267–277.

Butler, K. M. & Farrell, B. F. 1992 Three-dimensional optimal perturbations in viscous shear flow. *Phys. Fluids* A **4**, 637–650.

Cherubini, S., Robinet, J.-Ch. & Palma, P. De 2010 The effects of non-normality and nonlinearity of the Navier–Stokes operator on the dynamics of a large laminar separation bubble. *Phys. Fluids* **22**, 014102.

Ehrenstein, U. & Gallaire, F. 2008 Two-dimensional global low-frequency oscillations of a separating boundary layer flow. *J. Fluid Mech.* **614**, 315–327.

Eloy, C. & Le Dizes 1999 Three-dimensional instability of Burgers and Lamb–Oseen vortices in a strain field. *J. Fluid Mech.* **378**, 145–166.

Griffith, M. D., Leweke, T., Thompson, M. C. & Hourigan, K. 2008 Steady inlet flow in stenotic geometries: Convective and absolute instabilities. *J. Fluid Mech.* **616**, 111–133.

Griffith, M. D., Thompson, M. C., Leweke, T. & Hourigan, K. 2010 Convective instability in steady stenotic flow: optimal transient growth and experimental observation. *J. Fluid Mech.* **655**, 504–514.

Hourigan, K., Thompson, M. C. & Tan, B. T. 2001 Self-sustained oscillations in flows around long blunt plates. *J. Fluids Struct.* **15**, 387–398.

Hwang, K. S., Sung, H. J. & Hyun, J. M. 2000 Visualizations of large-scale vortices in flow about a blunt-faced flat plate. *Exp. Fluids* **29** (2), 198–201.

Hwang, K. S., Sung, H. J. & Hyun, J. M. 2001 An experimental study of large-scale vortices over a blunt-faced flat plate in pulsating flow. *Exp. Fluids* **30** (2), 202–213.

Jeong, J. & Hussain, F. 1995 On the identification of a vortex. *J. Fluid Mech.* **285**, 69–94.

Julien, S., Ortiz, S. & Chomaz, J.-M. 2004 Secondary instability mechanisms in the wake of a flat plate. *Eur. J. Mech. B/Fluids* **23**(1), 157–165.

Kaiktsis, L., Karniadakis, G. E. & Orszag, S. A 1996 Unsteadiness and convective instabilities in two-dimensional flow over a backward-facing step. *J. Fluid Mech.* **321**, 157–187.

Karniadakis, G. Em. & Sherwin, S. J. 1999 *Spectral/HP Element Methods for CFD*, 1st edn. Oxford University Press.

Karniadakis, G. E. & Trintafyllou, G. S. 1992 Three-dimensional dynamics and transition to turbulence in the wake of bluff objects. *J. Fluid Mech.* **238**, 1–30.

Kiya, M. & Sasaki, K. 1985 The structure of large scale vortices and unsteady reverse flow in the reattaching zone of a turbulent separation bubble. *J. Fluid Mech.* **154**, 463–491.

Kiya, M., Sasaki, K. & Yasakawa, M. 1983 Three dimensional structure of leading edge separation bubble. In *Proceedings of the Annual Meeting of the Hokkaido District of JSME*, no. 832-3, pp. 39–44.

Landman, M. J. & Saffman, P. G. 1987 The three-dimensional instability of strained vortices in a viscous fluid. *Phys. Fluids* **30**, 2339–2342.

Lane, J. C. & Loehrke, R. I. 1980 Leading-edge separation from a blunt plate at low Reynolds number. *Trans. ASME J. Fluid Engng* **102** (11), 494–496.

Leontini, J. S., Thompson, M. C. & Hourigan, K. 2007 Three-dimensional transition in the wake of a transversely oscillating cylinder. *J. Fluid Mech.* **577**, 79–104.

Leweke, T. & Williamson, C. H. K. 1998*a* Cooperative elliptic instability of a vortex pair. *J. Fluid Mech.* **360**, 85–119.

Leweke, T. & Williamson, C. H. K. 1998*b* Three-dimensional instabilities in wake transition. *Eur. J. Mech. B/Fluids* **17**, 571–586.

Marquet, O., Lombardi, M., Chomaz, J.-M., Sipp, D. & Jacquin, L 2009 Direct and adjoint global modes of a recirculation bubble: lift-up and convective non-normalities. *J. Fluid Mech.* **622**, 1–21.

Marquet, O., Sipp, D., Chomaz, J.-M. & Jacquin, L. 2008 Amplifier and resonator dynamics of a low-Reynolds-number recirculation bubble in a global framework. *J. Fluid Mech.* **605**, 429.

Mills, R., Sheridan, J. & Hourigan, K. 2003 Particle image velocimetry and visualization of natural and forced flow around rectangular cylinders. *J. Fluid Mech.* **478**, 299–323.

Nakamura, Y., Ohya, Y. & Tsurata, H. 1991 Experiments on vortex shedding from flat plates with square leading and trailing edges. *J. Fluid Mech.* **222**, 437–447.

Ohya, Y., Nakamura, Y., Ozone, S., Tsuruta, H. & Nakayama, R. 1992 A numerical study of vortex shedding from flat plates. *J. Fluid Mech.* **236**, 445–460.

Ota, T., Asano, Y. & Okawa, K. 1981 Reattachment length and transition of the separated flow over blunt flat plates. *Bull. JSME* **24** (192), 941–947.

Ozono, S., Ohya, Y., Nakamura, Y. & Nakayama, R. 1992 Stepwise increase in the Strouhal number for flows around flat plates. *Intl J. Numer. Meth. Fluids* **15**, 1025–1036.

Patera, A. T. 1984 A spectral element method for fluid dynamics: Laminar flow in a channel expansion. *J. Comp. Phys.* **54**, 468–488.

Reddy, S. C. & Henningson, D. S. 1993 Energy growth in viscous channel flows. *J. Fluid Mech.* **252**, 209.

Ryan, K., Thompson, M. C. & Hourigan, K. 2005 Three-dimensional transition in the wake of elongated bluff bodies. *J. Fluid Mech.* **538**, 1–29.

Sasaki, K. & Kiya, M. 1991 Three-dimensional vortex structure in a leading-edge separation bubble at moderate Reynolds numbers. *J. Fluids Engng* **113**, 405–410.

Sheard, G. J., Thompson, M. C. & Hourigan, K. 2003 From spheres to circular cylinders: the stability and flow structures of bluff ring wakes. *J. Fluid Mech.* **492**, 147–180.

Sheard, G. J., Thompson, M. C. & Hourigan, K. 2004 From spheres to circular cylinders: Non-axisymmetric transition in the flow past rings. *J. Fluid Mech.* **506**, 45–78.

Sigurdson, L. W. 1995 The structure and control of a turbulent reattaching flow. *J. Fluid Mech.* **298**, 139–165.

Sigurdson, L. W. & Roshko, A. 1984 The large-scale structure of a turbulent reattaching flow. *Bull. Am. Phys. Soc.* **29**, 1542.

Tafti, D. K. & Vanka, S. P. 1991 A numerical study of flow separation and reattachment on a blunt plate. *Phys. Fluids* **3**, 1749–1759.

Tan, B. T., Thompson, M. C. & Hourigan, K. 1998 Simulated flow around long rectangular plates under cross flow perturbations. *Intl J. Fluid Dyn.* **2** (1).

Tan, B. T., Thompson, M. C. & Hourigan, K. 2004 Flow past rectangular cylinders: receptivity to transverse forcing. *J. Fluid Mech.* **515**, 33–62.

Thompson, M. C. 2010 Transient growth of perturbations in the otherwise steady flow over a square leading edge plate. *J. Fluid Mech.* (submitted).

Thompson, M. C., Hourigan, K. & Sheridan, J. 1996 Three-dimensional instabilities in the wake of a circular cylinder. *Exp. Therm. Fluid Sci.* **12**, 190–196.

Thompson, M. C., Leweke, T. & Provansal, M. 2001*a* Kinematics and dynamics of sphere wake transition. *J. Fluids Struct*. **15**, 575–585.

Thompson, M. C., Leweke, T. & Williamson, C. H. K. 2001*b* The physical mechanism of transition in bluff body wakes. *J. Fluids Struct*. **15**, 607–616.

Trefethen, L. N., Trefethen, A. E., Reddy, S. C. & Driscoll, T. A. 1993 Hydrodynamic stability without eigenvalues. *Science* **261**, 578–584.

Waleffe, F. 1990 On the three-dimensional instability of strained vortices. *Phys. Fluids* A **2**, 76–80.

Williamson, C. H. K. 1996 Three dimensional wake transition. *J. Fluid Mech*. **328**, 345–407.

Wu, J., Sheridan, J., Welsh, M. C. & Hourigan, K. 1996 Three-dimensional vortex structures in a cylinder wake. *J. Fluid Mech*. **312**, 201–222.